

# Molecular Dynamics Study of Interfacial Cohesive Zone Law: Elastic Constant Effects

X. W. Zhou<sup>1,\*</sup>, N. R. Moody<sup>2</sup>, R. E. Jones<sup>1</sup>, J. A. Zimmerman<sup>1</sup>, E. D. Reedy<sup>3</sup>

<sup>1</sup> Mechanics of Materials Department, Sandia National Laboratories, Livermore, CA 94550, USA

<sup>2</sup> Analytical Materials Science Department, Sandia National Laboratories, CA 94550, USA

<sup>3</sup> Applied Mechanics Development Department, Sandia National Laboratories, Albuquerque, NM 87185, USA

**ABSTRACT:** A cohesive zone, finite element fracture analysis is based upon a traction-separation relation. Our recent work has used molecular dynamics simulations to derive general traction-separation relationships for interfacial fracture between two brittle materials under mix-mode loading conditions. Here we apply our method to explore the effects of elastic constants of the two materials on the traction-separation relationship. A comparison and discussion of our results will be provided.

## 1. INTRODUCTION

Modern approaches to the modeling and simulation of interfacial fracture use a cohesive zone model that defines the relation between traction and crack opening displacement [1]. Because experimental measurement of traction and crack opening at the crack tip is difficult, specific cohesive zone laws are often assumed rather than predicted. Recent advances in atomistic simulation methods have enabled attempts to derive the cohesive zone law from physics-based models [2,3]. We recently developed a molecular dynamics (MD) based approach to model fracture between two brittle materials under any combination of far field tensile (mode I) and shear (mode II) strains, and derived directly analytical functions relating local traction, local displacement, and local loading mode mixity [4]. Previous results from this analysis suggest that the work of separation depends on the elastic constant mismatch between the two materials, especially at the near-shear loading condition [5]. However, it is not clear if this dependence was caused by elastic constant mismatch alone or combination of elastic constant mismatch and the magnitude of the elastic constants. Here we perform additional simulations to address this issue.

## 2. METHODS

Our MD model is based on pairwise interatomic potentials for body-centered-cubic (bcc) materials. For an A-B binary system containing an A/B interface, three pair potential functions are needed respectively for A-A, B-B, and A-B interactions. Previous work [5] has developed five pair potential functions  $\phi_a(r)$ ,  $\phi_b(r)$ , ...,  $\phi_e(r)$  that have the same lattice constant and cohesive energy but different elastic constants. Here we assemble from these five pair functions four sets of potentials P1, P2, P3, and P4 for the binary A-B

---

\* Email: xzhou@sandia.gov

system. The correspondence of the A-A, B-B, and A-B interactions to the  $\phi_a$  -  $\phi_e$  functions are shown in Table 1 for potentials P1 – P4. The corresponding lattice constants, cohesive energies, elastic properties, and work of adhesion [5] are also shown. Note that potentials P1 and P2 have been used in the previous work [5] whereas potentials P3 and P4 are new additions.

**Table 1: Lattice constant  $a$  ( $\text{\AA}$ ), cohesive energy  $E_c$  (eV/atom), elastic constants  $C_{11}$ ,  $C_{12}$ , and  $C_{44}$  (eV/ $\text{\AA}^3$ ), Young's and shear moduli  $E$  and  $G$  (GPa), Poisson's ratio  $\nu$ , and work of adhesion  $wo_a$  (J/m $^2$ ), predicted by potentials P1 – P4**

		function	$a$	$E_c$	$C_{11}$	$C_{12}$	$C_{44}$	$E$	$G$	$\nu$	$wo_a$
P1	A-A	$\phi_a$	3.162	-4.45	3.25	1.15	1.15	444	177	0.25	5.968
	B-B	$\phi_a$	3.162	-4.45	3.25	1.15	1.15	444	177	0.25	5.968
	A-B	$\phi_d$	3.162	-1.78	1.26	0.48	0.48	177	71	0.25	2.336
P2	A-A	$\phi_b$	3.162	-4.45	3.41	1.21	1.21	466	186	0.25	5.968
	B-B	$\phi_c$	3.162	-4.45	1.64	0.57	0.57	222	89	0.25	6.032
	A-B	$\phi_e$	3.162	-1.78	0.46	0.33	0.33	72	28	0.30	2.400
P3	A-A	$\phi_a$	3.162	-4.45	3.25	1.15	1.15	444	177	0.25	5.968
	B-B	$\phi_a$	3.162	-4.45	3.25	1.15	1.15	444	177	0.25	5.968
	A-B	$\phi_e$	3.162	-1.78	0.46	0.33	0.33	72	28	0.30	2.400
P4	A-A	$\phi_c$	3.162	-4.45	1.64	0.57	0.57	222	89	0.25	6.032
	B-B	$\phi_c$	3.162	-4.45	1.64	0.57	0.57	222	89	0.25	6.032
	A-B	$\phi_e$	3.162	-1.78	0.46	0.33	0.33	72	28	0.30	2.400

The geometry of the system used in our MD simulations of crack propagation is shown in Fig. 1. The crystal contains 253 unit cells in the x- [100] direction, 206 unit cells in the y- [010] direction, and 10 unit cells in z- [001] direction, for a total of 1,042,360 atoms. Periodic boundary conditions were used in both x- and z- directions, and non-periodic boundary conditions were applied in the y- direction. As shown in Fig. 1, the top half of the crystal is composed of atoms A that fall into regions marked as 1 and 3, and the bottom half of the crystal is composed of atoms B that fall into regions marked as 2 and 4. Atoms that are marked black are boundary atoms through which tensile and shear loads were applied.

A crack in the middle of the A/B interface with an initial length around 28 nm was created by turning off the interactions between regions 1 and 2. To prevent the crack from being healed during shear deformation, we initiate atom neighbors at the start of the simulations and do not redetermine neighbors. During simulations of mode I crack propagation, the system is uniformly stretched (by moving each atom a distance corresponding to a uniform normal strain increment) in the y- direction each time step. During simulations of mode II crack propagation, the upper and lower halves of the vertical layer of black (boundary) atoms are displaced by a small distance in opposite directions along the x axis each time step. Numerical approaches are then used to update the atom positions based upon interatomic potential and Newton's equations of motion under the condition that the y coordinates of the top and bottom horizontal layers of black atoms and the x coordinates of the vertical layer of black atoms remain fixed. All

simulations were carried out at a constant temperature of 300 K, fixed system dimensions in the x- and z- directions, and constant strain rate.

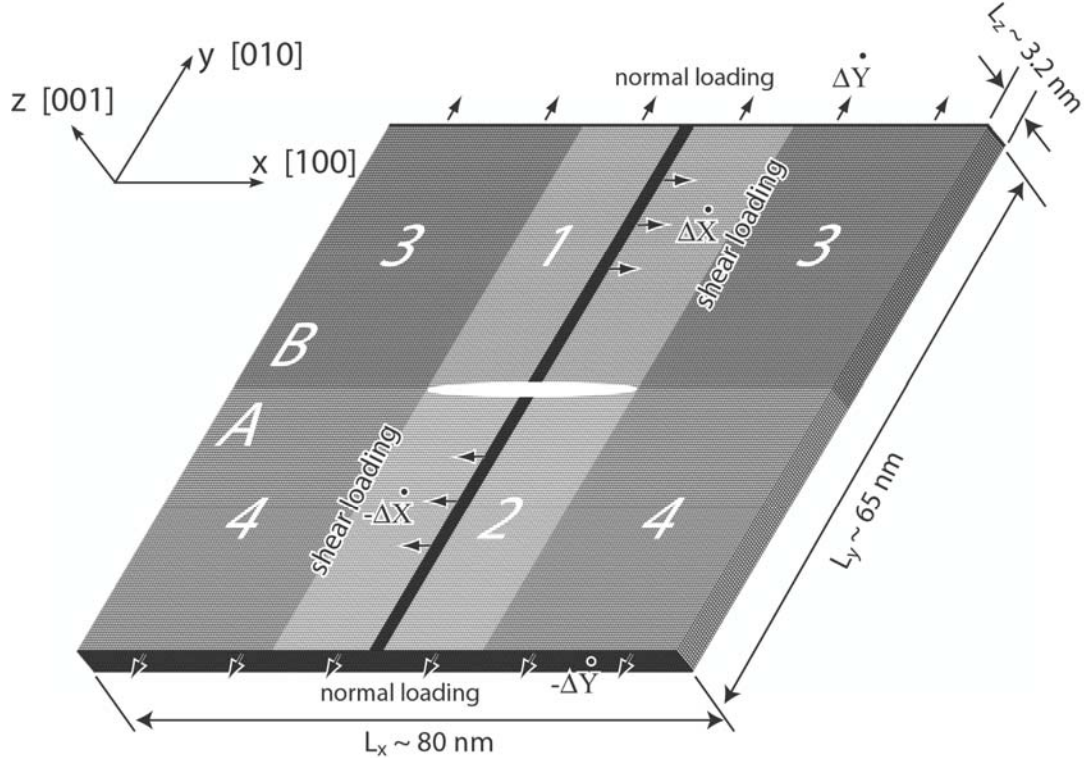


Fig. 1. Geometry of molecular dynamics simulation.

### 3. RESULTS

#### 3.1. Stress – strain curves and crack propagation dynamics

MD simulations of mode I (tensile) and mode II (shear) crack propagation were carried out for all four sets of potentials at constant boundary displacement rates  $\Delta\dot{X}$  and  $\Delta\dot{Y}$  in the x- and y- direction (see Fig. 1). The tensile and shear strain rates were defined by  $\dot{\varepsilon}_{yy} = 2\Delta\dot{Y}/L_y$  and  $\dot{\varepsilon}_{xy} = 2\Delta\dot{X}/L_y$ , respectively, where  $L_y$  is the sample dimension in the y- direction. The strain rates were chosen for each case so that the crack started to propagate at the late stage of the simulations. The strain rates used for different runs are shown in Table 2.

**TABLE 2: Shear  $\dot{\gamma}_{xy}$  and normal  $\dot{\varepsilon}_{yy}$  strain rates (unit  $10^8/\text{s}$ ) for different runs.**

Loading	$\dot{\gamma}_{xy} / \dot{\varepsilon}_{yy}$			
	Potential P1	Potential P2	Potential P3	Potential P4
Mode I	0.0/1.1	0.0/1.3	0.0/1.1	0.0/1.6
Mode II	2.0/0.0	1.9/0.0	1.8/0.0	2.1/0.0

The Virial theorem [6] was used to estimate global normal ( $\sigma_{yy}$ ) and shear ( $\sigma_{xy}$ ) stresses applied to the system. To reduce thermal oscillation, values of stress and strain were averaged over 10 time steps (each time step is 0.001 ps). Results of normal stress vs. normal strain curves obtained from the mode I simulations are shown in Fig. 2(a), and results of shear stress vs. shear strain curves obtained from the mode II simulations are shown in Fig. 2(b).

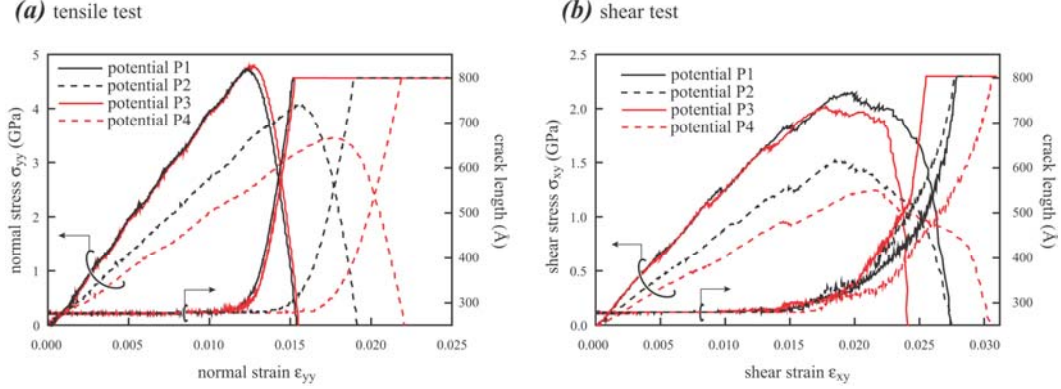


Fig. 2. Stress and crack length as a function of strain.

Fig. 2(a) indicates that during the tensile test, the normal stress initially increases linearly, corresponding to an elastic deformation of the system. The overall tensile elastic modulus seen from Fig. 2(a) is about 390 GPa for potentials P1 and P3, 270 GPa for potential P2, and 200 GPa for potential P4. For two materials A and B with the same height, the overall elastic modulus can be calculated as  $M = 2M_AM_B / (M_A + M_B)$ , where M can be the tensile (e.g.,  $C_{11}$ , E etc.) or shear (e.g.,  $C_{44}$ , G) modulus and the subscripts A and B refer to material. The overall elastic modulus estimated from  $C_{11}$  in Table 1 is about 520 GPa for potentials P1 and P3, 354 GPa for potential P2, and 262 GPa for potential P4. Note that the data listed in Table I were obtained at a temperature of 0 K whereas the values estimated from Fig. 2(a) are at 300 K at the presence of a crack. Nonetheless, the values estimated from Fig. 2(a) have the same trend as those in Table 1. In particular, the values estimated from Fig. 2(a) are seen to be about 75% of the values derived from Table 1 for all the potentials.

After the normal stress reaches the maximum, it starts to decrease towards zero as the strain further increases, signifying a possible fracture. It can be seen that the maximum stress is approximately  $\sigma_{\max} \approx 4.7$  GPa for potentials P1 and P3, 4.0 GPa for potential P2, and 3.4 GPa for potential P4. The critical strain at which the maximum stress occurs is approximately  $\epsilon_c \approx 0.0124$  for potentials P1 and P3, 0.0157 for potential P2, and 0.0180 for potential P4. The average, nominal strain energy density prior to the apparent fracture, defined as  $E_f = \sigma_{\max} \cdot \epsilon_c / 2$ , was calculated to be  $0.030 \text{ GJ/m}^3$  for potentials P1 and P3,  $0.033 \text{ GJ/m}^3$  for potential P2, and  $0.031 \text{ GJ/m}^3$  for potential P4. This probably reflects, at least in part, that all systems have the same interfacial work of adhesion as shown in Table 1.

A similar trend can be found in Fig. 2(b) for the shear test. The overall shear modulus estimated from the initial elastic deformation is estimated to be approximately 123 GPa

for potentials P1 and P3, 86 GPa for P2, and 76 GPa for potential P4. It should be noted that our shear loading is applied through the displacement of the vertical layer of boundary atoms as shown in Fig. 1. Such an approach is necessary to isolate out the crack phenomenon from the slip phenomenon [4]. While the way in which the stress is introduced should not affect the local traction vs. crack opening displacement relation, this loading would not generate a uniform shear stress if the interface was uncracked. Consequently, the estimated shear modulus cannot be directly compared with the  $C_{44}$  values listed in Table 1. However, the results are consistent as both Fig. 2(b) and Table 1 show a decreasing order for the shear modulus from potentials P1/P3, P2 to P4. The maximum fracture shear stress is seen to be approximately  $\tau_{\max} \approx 2.1$  GPa for potentials P1 and P3, 1.5 GPa for potential P2, and 1.2 GPa for potential P4, again showing a reduction of fracture stress due to a reduction of elastic modulus. We did not compare the critical strain and stored energy due to our special definition of the strain.

To examine the correlation between the observed stress vs. strain curves and fracture, crack length as a function of strain were calculated using the previous approach [5] and the results are included in Fig. 2 for both tensile and shear tests. It can be seen that crack did not propagate during the linear elastic deformation stage. When the stress reached the maximum value, the crack began to propagate. The crack then grew monotonically with increasing nominal applied strain.

### 3.2. Local traction and crack opening displacement

Following the approach used previously [5], a large number of local traction vs. crack opening data points (measured at different locations and times) were obtained during crack propagation of each MD run. These data points were averaged using an opening displacement bin size of 0.2 Å. The average tensile traction vs. crack normal opening displacement data obtained from the tensile tests, and the average shear traction vs. crack shear opening displacement data obtained from the shear tests, are shown respectively in Figs. 3(a) and 3(b) for all potentials. Fig. 3 generally agrees well with the previous results [4,5], especially as it also shows the double peak for the shear case. Unlike the previous work [5], Fig. 3 allows us to examine the effects of both elastic constant (but  $M_A = M_B$ ) and elastic constant mismatch ( $M_A \neq M_B$ ). Here we focus on the shear case where the elastic constants are seen to have a more significant effect. Comparison between the results from potentials P1 and P3 indicates that for systems where the elastic constants of A and B remain unchanged, a reduction of the interfacial stiffness between A and B causes a slight reduction of the local traction vs. local opening curves, although this causes a negligible effect on the global elastic behavior due to the minor interfacial volume fraction (see Fig. 2). Comparison between results from potentials P3 and P4 indicates that even when there is no elastic constant mismatch, a reduction in elastic modulus reduces the magnitude of the local traction generated by the local opening. Likewise, comparison between results from potentials P1 and P2 does show that elastic constant mismatch also reduces the magnitude of the local tractions.

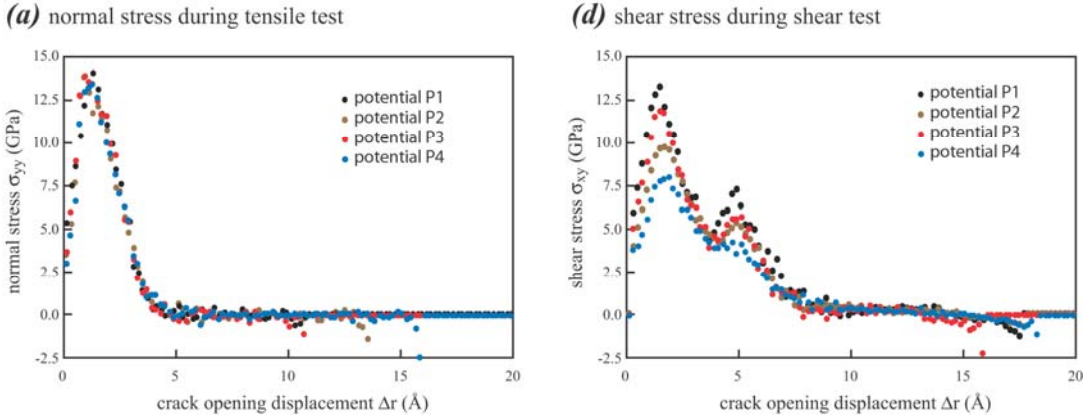


Fig. 3. Traction as a function of displacement obtained from MD simulations.

Fracture toughness can be defined by the work of separation as follows:

$$w = w(\psi) = \int_0^\infty \sigma_{yy} \cdot d(\Delta y) + \int_0^\infty \sigma_{xy} \cdot d(\Delta x) \quad (1)$$

By integrating Eq. (1), the work of separation was calculated with the results shown in Table 3. It can be seen that for the systems simulated, the mode II fracture generally has a higher toughness than mode I fracture. Consistent with the elastic constant effects observed in Fig. 3(b), the work of separation decreases from potential P1, P3, P2, to P4. The same trend can now be numerically seen for the tensile case, albeit less significantly.

**TABLE 3: Work of separation (J/m<sup>2</sup>) for different runs.**

Loading	Potential P1	Potential P2	Potential P3	Potential P4
Mode I	3.02	2.87	2.92	2.86
Mode II	4.81	3.86	4.13	3.31

#### 4. CONCLUSIONS

Systematic molecular dynamics simulations have been carried out to study the effects of elastic constants on the traction-separation relationship defining crack propagation between two brittle materials A and B. The simulations show that elastic constants have a noticeable effect on the local traction vs. crack opening relationship especially for the shear case where the local traction vs. crack opening curves may be reduced by either a reduction of the cross elastic constant between A and B (which has a minor effect on the global elastic properties), a reduction of the elastic constants of A and B, and an increase in the interfacial elastic mismatch. For the systems simulated, the mode II fracture has a higher work of separation than the mode I fracture.

#### 5. ACKNOWLEDGEMENTS

Sandia is a multi-program laboratory operated by Sandia Corporation, a Lockheed Martin

Company, for the United States Department of Energy's National Nuclear Security Administration under contract DEAC04-94AL85000.

## 6. REFERENCES

- 
- [1] X. P. Xu, and A. Needleman, *J. Mech. Phys. Solids*, **42**, 1397(1994).
  - [2] D. Spearot, K. Jacob, D. McDowell, *Mech. Mater.*, **36**, 825(2004).
  - [3] V. Yamakov, E. Saether, D. R. Phillips, E. H. Glaessgen, *J. Mech. Phys. Sol.*, **54**, 1899(2006).
  - [4] X. W. Zhou, J. A. Zimmerman, E. D. Reedy Jr., and N. R. Moody, *Mech. Mater.*, **40**, 832(2008).
  - [5] X. W. Zhou, N. R. Moody , R. E. Jones, J. A. Zimmerman, and E. D. Reedy Jr., *submitted to Acta Mater.*
  - [6] J. Zimmerman J, E. Webb III, J. Hoyt, R. Jones, P. Klein, and D. Bammann, Modell. *Simul. Mater. Sci. Eng.*, **12**, S319(2004).